On the Role of Coastal Troughs in the Circulation of Warm Circumpolar Deep Water on Antarctic Shelves

Pierre St-Laurent * John M. Klinck and Michael S. Dinniman

Center for Coastal Physical Oceanography, Norfolk, Virginia

* *Corresponding author address:* Pierre St-Laurent, Center for Coastal Physical Oceanography, 4111 Monarch Way, Norfolk, VA 23529.

E-mail: pierre@ccpo.odu.edu

ABSTRACT

Oceanic exchanges across the continental shelves of Antarctica play an important role in biological systems and the mass balance of ice sheets. The focus of this study is on the mechanisms responsible for the circulation of warm Circumpolar Deep Water (CDW) within troughs running perpendicular to the continental shelf. This is examined using process-oriented numerical experiments with an eddy-resolving (1 km) 3–D ocean model that includes a static and thermodynamically active ice shelf. Three mechanisms that create a significant onshore flow within the trough are identified: (1) a deep onshore flow driven by the melt of the ice shelf, (2) interaction between the longshore mean flow and the trough, and (3) interaction between a Rossby wave along the shelf break and the trough. In each case the onshore flow is sufficient to maintain the warm temperatures underneath the ice shelf and basal melt rates of $O(1\,\mathrm{m\,yr^{-1}})$. The third mechanism in particular reproduces several features revealed by moorings from Marguerite Trough (Bellingshausen Sea): the temperature maximum at mid-depth, a stronger intrusion on the downstream edge of the trough, and the appearance of warm anticyclonic anomalies every week. Sensitivity experiments highlight the need to properly resolve the small baroclinic radii of these regions (5 km on the shelf): simulations at 3 km resolution cannot reproduce mechanism 3 and the associated heat transport.

1. Introduction

Several studies provide evidence of an accelerating flow of the Greenland and Antarctic ice sheets over the last 10 years (Joughin et al. 2008; Pritchard et al. 2009; Rignot et al. 2011). Different mechanisms have been proposed to explain the mass loss but the processes taking place at the floating extensions of the ice sheets (ice shelves) seem to act as a trigger in many cases (Nick et al. 2009; Payne et al. 2004). One hypothesis is that sub-ice shelf melting plays an important role in the mass loss (e.g., Holland et al. 2008a). It is particularly plausible in Antarctica where the large-scale atmospheric forcing raises the deep warm water (Circumpolar Deep Water, CDW) to the level of the continental shelf. Such warm water (potential temperature $1 < \theta < 2°$C, or up to $4°$ above *in situ* freezing point θ_{f}) are present in several locations of the continental shelf of western Antarctica (Jenkins and Jacobs 2008; Klinck et al. 2004; Martinson and McKee 2012; Moffat et al. 2009; Wåhlin et al. 2010; Walker et al. 2007) and within some water cavities beneath the floating ice shelves (e.g., Jenkins et al. 2010). Apart from their potential role in the mass balance of ice sheets, cross-shelf exchanges of CDW are also known to impact biological systems significantly (Prézelin et al. 2000).

The processes responsible for the transport of CDW across the shelf break and continental shelf remain elusive. At the low Rossby numbers that characterize large-scale ocean currents, the flow direction is along the shelf break (i.e. along lines of constant linearized potential vorticity f/H; f is Coriolis parameter and H depth) and cross-shelf exchanges are thus limited. Klinck and Dinniman (2010) propose a number of mechanisms for cross-shelf exchanges: (1) Ekman transport in the bottom layer, (2) deviation of the zonal flow by bottom corrugations (Dinniman et al. 2003; Dinniman and Klinck 2004), (3) upward displacement of isotherms due to an accelerating Antarctic Circumpolar Current (ACC), (4) eddy fluxes driven by instabilities (e.g., Nøst et al. 2011; Zhang et al. 2011a), (5) atmospheric forcing, and (6) formation of a buoyancy-driven cell. The relative importance of these mechanisms is most likely location-dependent and would vary according to several parameters, notably the position of the ACC relative to the shelf break.

Nevertheless, recent observations suggest that troughs running across the southern extension of the ACC are particularly effective at channeling warm water toward ice shelves in the Amundsen and Bellingshausen seas (Walker et al. 2007; Moffat et al. 2009; Wåhlin et al. 2010). The mooring arrays described by Moffat et al. (2009) and Martinson and McKee (2012) captured several features of such warm intrusions. First, CDW is mostly found within the trough and other bathymetric depressions. The flow within the trough is onshore and has a mean velocity of $5\,\mathrm{cm\,s^{-1}}$ with eddy-like events that are embedded within the mean flow. The events are of small spatial scales (comparable to the local Rossby radius, 5 km) and they frequently cross the mooring array (about four times per month). These intrusions are much more frequent on the eastern (downstream) side of the trough.

Some of these features are successfully reproduced in numerical simulations with 3–D sea ice-ocean coupled models. The simulations of Dinniman et al. (2011) show CDW being effectively advected within the large troughs fringing the shelf of the Ross and Bellingshausen seas. Interestingly, the authors note a significant correlation ($R = 0.44$) between longshore winds upstream of a trough and the flux of CDW within the trough. The periodicity and duration of these intrusions are consistent with the data from Moffat et al. (2009). On the other hand, the model resolution (4 km) only resolves the larger troughs, and the potentially important eddy-like events described by Moffat et al. (2009) cannot be reproduced at such model resolution.

This study aims to complement the scarce observations and previous modeling efforts at coarse resolutions (e.g. Hellmer et al. 2012; Steig et al. 2012) by describing process-oriented simulations of cross-shelf exchanges in the presence of a trough. The horizontal resolution of the model (1 km) is sufficient to explicitly resolve the potentially important mesoscales. The specific objectives are: (1) to identify the mechanisms responsible for the onshore transport of warm CDW and (2) to estimate the onshore heat transport associated with each of these mechanisms. We examine these issues with a model configuration representative of the continental shelf in the Bellingshausen Sea and west Antarctic Peninsula (wAP).

2. Theory

a. *Heat Budget for Warm Antarctic Continental Shelves*

Continental shelves in western Antarctica are characterized by anomalously warm ocean temperatures ($\theta - \theta_\mathrm{f} \sim 3$°C, see Nicholls et al. 2009, their Fig. 1). Conditions inside the ice cavities are more difficult to observe, but recent data from the Amundsen Sea reveal that the water with access to the grounding zone (the point where the ice shelf meets the solid ground) has properties that are very similar to those 400 km offshore (Jacobs et al. 2011, their Fig. 2). This suggests a strong circulation of warm water that reaches inside the cavity and maintains its mean temperature close to that of the inflow. It will be shown in the next sections that the melt of the ice shelf and the circulation on the shelf are, in this limit, mostly uncoupled.

The thermodynamics of warm ice cavities was investigated previously by Little et al. (2009). Their model domain is limited to the ice cavity and the external ocean conditions (temperature and salinity) that drive the melt are prescribed at a given distance from the grounding zone. In simulations with warm ambient waters $\theta = 1.5$°C, the melt rate is primarily limited by the entrainment (vertical mixing) of heat from the deep warm layer to the under-ice boundary layer, and this entrainment strongly depends on the slope (geometry) of the ice shelf (Little et al. 2009).

In this study we are primarily interested in the circulation of CDW water on warm continental shelves. A convenient metric for this circulation is the onshore heat transport defined as:

$$\mathrm{OHT}(y,t) \equiv \int_{-H}^{0} \int_{-Lx}^{Lx} -v\,\mathcal{H}(-v)\ (\theta - \theta_\mathrm{f})\ \rho_0\, c_p \,\mathrm{d}x\,\mathrm{d}z \qquad (1)$$

where $-Lx < x < Lx$ is the along-shelf extent of the model domain, v is the seaward component of velocity, $\mathcal{H}(-v)$ is the Heaviside function worth 1 for onshore flow and zero otherwise, ρ_0 a density reference, and $c_p = 4 \times 10^3\,\mathrm{J\,(kg\,K)^{-1}}$ the specific heat. A large OHT implies that the waters offshelf and onshelf are closely connected by the exchanges within the trough.

The conditions on cold continental shelves differ considerably from those of west Antarctica. Easterly winds and coastal downwelling (Sverdrup 1953), surface heat loss to sea ice and the atmosphere, and strong katabatic winds contribute to a very distinct temperature front ($\Delta\theta > 1.75°$C) separating warm CDW offshelf and near-freezing waters onshelf (e.g., Nøst et al. 2011, their Fig. 1). In contrast, wind reanalyses (NCAR 2010) and cross-shelf transects (Moffat et al. 2009) reveal weak onshore winds in the Bellingshausen Sea and a small temperature gradient $\Delta\theta \sim 0.3°$C between onshelf and offshelf waters.

b. Cross-Shelf Exchanges in Presence of Cross-Shelf Topography

A good description of the response of a stratified flow U to topography is provided by Fennel and Schmidt (1991). These authors solve the non-linear quasigeostrophic equation and derive analytical solutions for the cases of a trough infinite in the cross-stream direction (y) and for a circular abyss (a trough of finite length would share features from these two limiting cases). The two scenarios follow a similar evolution. In the early stage ($t < L/U$, L being a length scale for the topography), vortex stretching (squashing) of the deeper layers take place on the upstream (downstream) side of the trough and generate a cyclonic (anticyclonic) vortex (e.g., Huppert and Bryan 1976, their Fig. 2). After a transient period $t > L/U$, the downstream vortex is eventually advected with the mean flow and the upstream vortex occupies the whole trough. Topographic waves are also generated if the trough has a finite length and they propagate along the isobaths that act as waveguides. Their period is given by (Fennel and Schmidt 1991):

$$T_{\text{top}} = \frac{4\pi\, H_0}{f\, H_{\text{trough}}} \left[1 - \frac{2R_1}{a} \ln\left(2 - 2\cos\left[\frac{\pi\, H_{\text{trough}}}{H_0}\right]\right)\right]^{-1}, \tag{2}$$

where H_0 is the depth of the continental depth, H_{trough} and a are scales for the depth and width of the trough, and R_1 is the first baroclinic Rossby radius. Using the half-depth and half-width of the trough for parameters H_{trough}, a gives a period $T_{\text{top}} \sim 5.4$ days.

A similar response to topography is described in the literature on ocean canyons. After an initial transient period, stretching in the deep layers in contact with the topography leads to a cyclonic circulation over the canyon (see Allen and Hickey 2010, for a review). The circulation involves the flow crossing isolines of f/H and this behavior is explained by momentum advection (see Allen and Hickey 2010, for a detailed analysis of the dynamics).

Another mechanism that can lead to cross-shelf exchanges within troughs is eddy-topography interactions. Zhang et al. (2011b, their Fig. 4) show how a Rossby wave propagating along-shelf breaks as it reaches the downstream edge of an embayment. The wave breaking process produces on average a net transport of properties in the cross-shelf direction. Similarly, Holloway (1992) proposes under a number of assumptions that the mean barotropic flow resulting from interactions among random eddies would be to the left of the topographic gradient $\boldsymbol{\nabla} H$ in the southern hemisphere ($f < 0$). For a trough in Antarctica, this means again a cyclonic circulation.

3. Method

a. Model Description

The numerical simulations are conducted with the ROMS ocean model (Regional Ocean Modeling System version 3.4; Shchepetkin and McWilliams 2008; Hedström 2009) that solves the 3–D hydrostatic Boussinesq primitive equations. The model domain is 600×300 km and represents an idealized coastal segment in western Antarctica. It includes a deep offshore area, a flat continental shelf, and an ice shelf cavity (Fig. 1). The depths are zonally uniform (except for the trough and ice shelf) and vary from 3000 m in the oceanic part to 500 m on the continental shelf, which matches conditions in the Bellingshausen Sea and west Antarctic

Peninsula. The ice shelf thickness is 400 m at the grounding line and linearly decreases to zero over a 110 km distance. Following Little et al. (2009), the sides of the cavity are smoothly tapered in the zonal direction rather than being straight walls. A trough is added to the continental shelf and provides a connection between the ice shelf cavity and the waters off the shelf break. The geometry of the trough approximately follows that of Marguerite Trough (40 km wide and 150 m deep, see Dinniman et al. 2011). The meridional variation of f is included in the model but it plays a negligible role compared to topographic variations. Lateral boundaries are set to no-slip.

The ice shelf is static but thermodynamically active so that it interacts with the ocean physics (see Dinniman et al. 2007). Both the mechanical (pressure, quadratic friction) and thermodynamical effects of the ice shelf on the waters beneath are included. Following Holland and Jenkins (1999), the heat and salt transfer coefficients are functions of the friction velocity. The vertical discretization of the ocean model has 32 topography-following (σ) levels concentrated near the surface and bottom, so that the dynamics underneath the ice shelf are relatively well resolved ($\Delta z \approx 3$ m at the grounding line). The horizontal resolution of the model is constant over the domain and equal to 1 km. Such high resolution is necessary to resolve the mesoscale structures given the small baroclinic Rossby radii (5 km on the shelf).

b. Forcings and Initial/Boundary Conditions

It is assumed as a first approximation that the system is primarily forced by the large-scale zonal flow observed in western Antarctica. This geostrophic flow corresponds to the southern part of the ACC and can be prescribed by setting the salinity (S) and potential temperature (θ) fields over the western and eastern open boundaries. The effect of the mean wind stress forcing is assumed to be included in these S, θ conditions. Local transient winds are neglected under the assumption that they would only contribute to transient perturbations from the mean geostrophic state. Similarly, sea ice is not included in these simulations since it is expected to have a weak influence on the flow (data from AMSR-E

(Advanced Microwave Scanning Radiometer, Cavalieri et al. 2004) show a mean ice cover of only 25% over the shelf break of the Bellingshausen Sea in 2010).

The initial and boundary conditions for S, θ are derived from vertical profiles taken across the shelf of the Bellingshausen Sea (Jenkins and Jacobs 2008, their Fig. 2). They show a deep ($\sim 100\,\mathrm{m}$) surface layer that is close to the freezing point and separated from a warm deep layer (CDW, $\theta > 1^\circ\,\mathrm{C}$) by a strong thermocline. The salinity profiles similarly show a stratified surface layer extending down to $300\,\mathrm{m}$ and a deep salty ($S > 34.7\,\mathrm{psu}$) layer underneath. How this vertical structure evolves in the cross-shelf direction is determined from a set of assumptions: (1) the zonal transport per unit width ($\overline{u}(y)\,H(y)$) is $300\,\mathrm{m^2\,s^{-1}}$ offshore (the overline denotes a vertical average) and smoothly goes to zero at the upper shelf break (Fig. 2). (2) The zonal flow is in geostrophic balance and vanishes at the sea bottom. (3) The isotherms and isohalines share the same slope. (4) The S, θ profiles can be approximated as piecewise linear functions of $S_{\mathrm{hc}}(y), \theta_{\mathrm{tc}}(y)$ (e.g., Holland et al. 2008b):

$$S(y,z) \equiv \begin{cases} S_1 & \text{if } z_1 < z < 0, \\ S_1 + (z_1 - z_2)^{-1}\,(z_1 - z)(S_{\mathrm{hc}}(y) - S_1) & \text{if } z_2 < z < z_1, \\ S_{\mathrm{hc}}(y) + (H_{\max} + z_2)^{-1}\,(z_2 - z)(S_2 - S_{\mathrm{hc}}(y)) & \text{if } -H(y) < z < z_2, \\ \text{where } S_1 = 32.9\,\mathrm{psu}, \quad S_2 = 35.0\,\mathrm{psu}, \quad S_{\mathrm{hc}}(y) = S(y, z = z_2), & \\ \qquad z_1 = -25\,\mathrm{m}, \quad z_2 = -350\,\mathrm{m}, & \end{cases} \tag{3}$$

$$\theta(y,z) \equiv \begin{cases} \theta_1 & \text{if } z_1 < z < 0, \\ \theta_1 + (z_1 - z_2)^{-1}\,(z_1 - z)(\theta_{\mathrm{tc}}(y) - \theta_1) & \text{if } z_2 < z < z_1, \\ \theta_{\mathrm{tc}}(y) + (H_{\max} + z_2)^{-1}\,(z_2 - z)(\theta_2 - \theta_{\mathrm{tc}}(y)) & \text{if } -H(y) < z < z_2, \\ \text{where } \theta_1 = -1.8^\circ\,\mathrm{C}, \quad \theta_2 = 0.5^\circ\,\mathrm{C}, \quad \theta_{\mathrm{tc}}(y) = \theta(y, z = z_2), & \\ \qquad z_1 = -100\,\mathrm{m}, \quad z_2 = -350\,\mathrm{m}, & \end{cases} \tag{4}$$

where the subscripts hc,tc refer to the halocline and thermocline. The four assumptions lead to two equations (prescribed $\overline{u}\,H$ and pressure gradient vanishing at bottom) for two unknowns ($(\partial\eta/\partial y)(y)$ and $S_{\mathrm{hc}}(y)$, where η is the sea surface elevation). The equation set is solved at each location y starting from $y = 0$.

The resulting fields (Fig. 2) can be compared to the S, θ transect measured by Jenkins and Jacobs (2008, their Fig. 2) and to geostrophic velocities estimated from density profiles (Fig. 3). The temperature at the grounding line is about three degrees above the *in situ* freezing point. The sloping bathymetry at the break causes the steepening of the isohalines and the formation of a shelf break jet (sbj) with maximum speeds $u = 0.5\,\mathrm{m\,s^{-1}}$ and $\overline{u} = 0.3\,\mathrm{m\,s^{-1}}$ (Fig. 2). These velocities are consistent with those obtained in realistic simulations of the Bellingshausen Sea (Dinniman et al. 2011). The sea surface elevation η varies between zero at the shelf break to 0.4 m at the northern boundary (Fig. 2). The density field produces a baroclinic Rossby radius of about 5 km on the shelf and up to 13 km offshore (Fig. 2).

These fields are used as the initial and boundary conditions of the model. The western and eastern boundaries are open while the northern side is a solid wall (Fig. 1). All variables are gradually relaxed toward the initial conditions within nudging zones that are 100 km wide. The relaxation timescale τ smoothly varies in the western nudging layer as (e.g., Nycander and Döös 2003, their Eq. B17):

$$\frac{1}{\tau} = \frac{1}{2\,\Delta t}\left[1 + \cos\left(\pi \frac{x}{100\,\mathrm{km}}\right)\right] \tag{5}$$

where x is the distance from the boundary and Δt is equal to 2 s for 2–D momentum and 1 day for 3–D momentum and tracers. A similar function is used at the eastern boundary.

c. *Simulations Conducted*

A total of 13 model simulations are conducted (Table 1) to examine the influence of each of these parameters: presence/absence of a trough, thermodynamical exchanges between the ocean and the base of an ice shelf, speed of the longshore flow, position of the maximum flow (y(jet)), and mesh size. In all these simulations the boundary conditions $S, \theta, \mathbf{u}$ are held constant in time and model fields are saved every 12 hours. Some of these simulations deserve further explanation. In Runs #3,4, the function $\overline{u}(y)\,H(y)$ is modified to represent a wide sbj that extends further inshore by 12 km (Fig. 2). This modification alone would yield levels of shear $\|\partial u/\partial z\|$ greatly exceeding those from the other runs (since H decreases toward the shore). To ease the comparison with the other runs, $\|\partial u/\partial z\|_{\max}$ is maintained at $8 \times 10^{-4}\,\mathrm{s}^{-1}$ by decreasing the value of $\overline{u}\,H$ offshore from 300 to $90\,\mathrm{m}^2\,\mathrm{s}^{-1}$ (Fig. 2). Finally, Runs #13–16 are used to determine the sensitivity of the onshore heat transport to variations in jet speed and jet position. Note that the explicit horizontal eddy viscosity is the same in all the simulations irrespective of the horizontal resolution Δx (harmonic $1\,\mathrm{m}^2\,\mathrm{s}^{-1}$).

4. Results

a. Basic Case: Circulation and Melt in Absence of Trough

We first examine the case of a continental shelf without a trough (Run #1). In such case, the dynamics on and off the shelf are independent: the jet (and the mesoscale structures associated with it) remain close to the shelf break, while the waters on the shelf are at rest except in the vicinity of the ice cavity. The deep warm water from the cavity initiates the melt of the ice shelf within the first few days of simulation. This melt acts to depress the isopycnals (that were initially flat, see Fig. 2) and increases the local stratification. The sloping isopycnals in turn generate by thermal wind a shallow westward flow and a deep eastward flow. The circulation over the neutral density surface $\gamma_2 \equiv 1027.8\,\mathrm{kg\,m}^{-3}$ well represents this deep circulation (Fig. 4; $z(\gamma_2) \sim -300\,\mathrm{m}$). Meridional flow mostly occurs along the side walls where lateral friction allows the fluid to cross f/H isolines (e.g., Little et al. 2008). The streamlines of the deep current gradually disappear along the southern side of the cavity as this deep water is being upwelled to upper layers.

The basal melt rate rapidly stabilizes (within 10 days of simulation) toward a constant value of $5.8\,\mathrm{m\,y}^{-1}$ (average over the area of the ice shelf). This vertical heat transfer from the ocean to the ice shelf is proportional to the temperature difference $\theta - \theta_{\mathrm{ice}} = \theta - \theta_{\mathrm{f}}$ (Holland and Jenkins 1999, θ_{ice} is the temperature at the base of the ice shelf and θ_{f} the *in situ* freezing point). The heat transfer varies spatially and the bulk (70%) of it takes place within 20 km of the grounding line. At the grounding line, the ice shelf is in direct contact with the warm bottom layer and the depression of θ_f with pressure contributes to 0.3°C in the temperature difference $\theta - \theta_\mathrm{f}$. Another factor contributing to the non-uniform basal melt pattern is a thin layer of fresh water that covers the whole ice shelf and shields it from the warm ambient waters except at the grounding line.

b. First Mechanism: Melt-Driven Flow inside the Trough

We now add to the basic model setup a trough connecting the ice cavity to the shelf break (Run #2). We focus on the deep layer of density γ_2 since it is representative of the warm bottom waters involved in the cross-shelf exchanges. Within the first days of simulation, the deep eastward flow described earlier is steered by the trough, veers northward, and leaves the ice cavity along the western edge of the trough. This outflow is compensated by another deep current that brings waters from the shelf break to the cavity along the middle of the trough. The mean circulation (Fig. 5) thus includes two sources of warm deep water to the cavity: first an inflow along the western wall of the cavity, and an inflow of shelf break waters coming along the trough.

The two sources contribute equally to the onshore heat transport that amounts to 2.6×10^{12} W at $y = 99$ km (40% higher than in Run #1; the transport is relative to *in situ* θ_f). Despite the higher heat inflow, the basal melt rate is similar to that of Run #1 (5.9 m y^{-1}). As mentioned previously, the melt rate in a warm cavity is not expected to depend directly on the onshore heat transport (see Section 2). The additional 40% simply circulates in and out of the cavity. The circulation over the upper layers and the spatial distribution of the basal melt are similar to the case without a trough (Fig. 4).

c. *Second Mechanism: Mean Flow-Topography Interaction*

A second mechanism for cross-shelf exchanges within the trough appears when we introduce a wide, eastward shelf break jet (sbj) that flows across the entrance of the trough (Run #3). For simplicity, we consider the idealized case where the friction velocity at the base of the ice shelf, $\sqrt{\boldsymbol{\tau}_{\mathrm{surf}}/\rho_0}$, is set to zero. This choice removes ice shelf thermodynamics as a driving mechanism and sets a free-slip condition at the ice shelf-ocean boundary. During the first five days of simulation, vortex stretching (squashing) forms a cyclonic (anticyclonic) vortex on the upstream (downstream) side of the trough (Fig. 6). Over the following days, the cyclonic vortex gradually takes over the trough and sets a dominantly cyclonic flow. This sequence is in agreement with the theoretical scenario of mean flow-topography interaction described by Fennel and Schmidt (1991), and qualitatively similar to the flow pattern in advection-driven canyon upwelling (see Section 2). As a result of this circulation, an onshore heat transport rapidly develops (within five days) along the trough. Its magnitude at $y = 99\,\mathrm{km}$ is of the same order of magnitude as for the previous mechanism ($\sim 3 \times 10^{12}\,\mathrm{W}$).

Superimposed on this circulation, a Rossby wave appears within the shelf break jet after ten days of simulation (Fig. 6) and propagates toward the east. The growth of such wave is expected since the jet is strongly sheared in the horizontal and vertical (Fig. 2) and thus unstable. Some mesoscale structures move onto the shelf and are advected within the trough. An important point however is that this mesoscale variability is not necessary for the development of the onshore heat flux in this simulation. An additional calculation (Run #4) was conducted at a coarser eddy-permitting resolution (3 km) and an intrusion (very similar) also develops. The onshore heat transport for Runs #3 and 4 are similar.

d. *Third Mechanism: Wave-Topography Interaction*

A different mechanism comes into play when the sbj is moved offshore so that the streamlines do not run directly over the entrance of the trough (Runs #5,6,7,11; see Fig. 2). The flow within the trough develops slowly and is dominated by topographic waves. The waves have a period of 7 ± 1 days (estimated from a y-t Hovmöller diagram and close to Eq. 2) and propagate cyclonically around the trough. This period approximately matches that of the Rossby wave (similar to the one of Run #3) that appears within the sbj after 10 days of simulation. The Rossby wave corresponds to cyclonic (low potential vorticity $q = (\zeta + f)/h$, where ζ is the relative vorticity and h the thickness $\delta\rho\, \partial z/\partial\rho$) and anticyclonic (high q) anomalies propagating eastward at about $5\,\mathrm{cm\,s^{-1}}$ (Fig. 7). The waters offshore (onshore) have higher (lower) q because the isopycnals deepen northward.

Within a few days of simulation the Rossby wave starts to break (the sign of $\partial q/\partial y$ reverses twice between $y = 200$ and $y = 225\,\mathrm{km}$; Fig. 7). The breaking of the wave is most intense over the eastern edge of the trough. At this location, the high q (anticyclonic) anomalies clearly separate from the shelf break in a way qualitatively similar to Zhang et al. (2011b, their Fig. 4). The warm (Fig. 8) anticyclones then follow lines of constant f/H by moving southward along the eastern edge of the trough. Over time, the accumulation of the anticyclonic anomalies forms a tongue that progresses onshore and eventually reaches the cavity after 80 days of simulation (Figs. 7,8).

The low-frequency circulation (obtained from a 20-day block average that filters the topographic waves, see Fig. 9) closely matches the development of the tongue. An onshore flow of speed $v \sim -5\,\mathrm{cm\,s^{-1}}$ takes place along the inner part of the trough and a return flow is apparent along the outer part. Note the absence of a cyclonic cell within the trough (compare Figs. 6,9). The onshore heat transport at $y = 99\,\mathrm{km}$ grows slowly and reaches $4 \times 10^{12}\,\mathrm{W}$ after 200 days of simulation. In contrast with the previous mechanisms, the cross-shelf exchanges of Mechanism 3 are sensitive to the model resolution. The onshore heat transport decreases by an order of magnitude (to $10^{11}\,\mathrm{W}$) if a coarser eddy-permitting resolution of $3\,\mathrm{km}$ is used (Run #6). This is a strong indication that mesoscales play an important role in this mechanism. Also, reducing the velocity of the jet from $0.58\,\mathrm{m\,s^{-1}}$ to $0.38\,\mathrm{m\,s^{-1}}$ ($0.19\,\mathrm{m\,s^{-1}}$) increases the stability of the jet and decreases the heat transport by 55% (80%; see Fig. 10). Similarly, moving the jet away from the trough inhibits the wave-topography interaction and the heat transport decays by an exponential factor for a displacement Δy of one Rossby radius (Fig. 10).

e. *Combined Effect of Thermodynamics, Shelf Break Jet, and Trough*

Run #7 combines the effect of ice shelf melt, the trough, and the sbj. The flow over the deep layer γ_2 that represents the warm water (Fig. 11) is qualitatively a superposition of the flow from Run #2 (melt-driven circulation, no sbj) and Run #5 (sbj, no melt). We notably recognize the cyclonic circulation within the cavity (associated with the melt-driven circulation), and the intrusion of warm anticyclonic anomalies (high ψ values) over the eastern side of the trough (due to the wave-topography interaction). There is a regularity (every 6.5 days) at which the warm anomalies appear at the entrance of the trough (Fig. 12) and it matches the propagation speed ($\sim 5\,\mathrm{cm\,s^{-1}}$) and wavelength ($\sim 2\pi \times 5\,\mathrm{km}$) of the Rossby wave along the shelf break.

The combination of these two mechanisms (melt-driven circulation and wave-topography interactions) leads after 100 days of simulation to intrusions on both sides of the trough, the intrusion on the eastern side being dominant. Overall the trough contributes to 75% of the onshore heat transport at $y = 99\,\mathrm{km}$, while the deep inflow on the western side of the cavity provides the remaining 25%. For comparison, 50% of the heat was supplied by the trough in the run without a sbj (Run #2). The onshore transport grows steadily over the duration of Run #7 (347 days) as the ice melt does not balance the onshore transport of ocean heat. The extra heat circulates in and out the cavity and the basal melt rate remains $5.9\,\mathrm{m\,y^{-1}}$ (see the next section for a detailed heat budget of Run #7).

f. Onshore Heat Transport

The heat transported to the ice cavity at $y = 99\,\mathrm{km}$ (Fig. 13) is a good diagnostic for the comparison of the different simulations. Mechanisms 1 and 2 (the buoyancy-driven circulation and the mean flow-topography interaction, Runs #2,4 respectively) both lead to an onshore heat transport that grows and stabilizes within a short period of time (20 days). This is in contrast to Mechanism 3 (wave-topography interaction, Run #5 and Fig. 9) where the onshore heat transport increases gradually during the simulation. The three mechanisms provide a similar amount of heat to the ice cavity after 140 days of simulation ($\sim 2.5 \times 10^{12}\,\mathrm{W}$, comparable to Walker et al. (2007)). Although the simulations were not designed to determine which of these mechanisms is the most effective in realistic conditions, the key result is that any of them can provide a significant amount of heat to the ice shelf. An important caveat is that Mechanism 3 is poorly captured in simulations with non-eddy resolving resolutions. The onshore heat transport at $t = 150$ days is approximately halved with $\Delta x = 2\,\mathrm{km}$, and becomes negligible with $\Delta x = 3\,\mathrm{km}$ (Fig. 13).

The depth-integrated heat content on the shelf (horizontally averaged between $y = 0$ and $180\,\mathrm{km}$, Fig. 13) provides an additional diagnostic. The curves cluster into two groups depending on the presence or absence of thermodynamics. Active thermodynamics cause a general decrease of about $30\,\mathrm{MJ\,m^{-2}}$ over the first 40 days. Also, the heat content increases slightly in all the simulations but this increase plays a small role in the heat budgets. For instance, the budget for the cavity of Run #7 (averaged between days 40–160) has a heat inflow $\sim 3.8 \times 10^{12}\,\mathrm{W}$, heat outflow $\sim 2.2 \times 10^{12}\,\mathrm{W}$, surface flux $\sim 1.4 \times 10^{12}\,\mathrm{W}$, and a temperature change $V_{\mathrm{cavity}} c_p \rho_0\, \partial\overline{T}/\partial t \sim 10^{11}\,\mathrm{W}$ (V_{cavity} is the volume of the ice shelf cavity). The majority of the heat inflow (75%) is from the through and the increase in the heat content of the continental shelf (Fig. 13) is also concentrated along the trough (Fig. 8) at mid-depth. For example, the temperature change $\Delta\theta$ between initial time and day 347 at $(x, y) = (300\,\mathrm{km}, 120\,\mathrm{km})$ is maximum at a depth of $310\,\mathrm{m}$ with $\Delta\theta = +0.3°\mathrm{C}$ (Run #7). The mean heat transport includes the contribution of warm anticyclonic anomalies (see

Section 4d) apparent in the standard deviation of the temperature field (Fig. 14). The anomalies are centered at mid-depth ($\sim 300\,\mathrm{m}$) in agreement with the observations of Moffat et al. (2009, their Fig. 11). Their horizontal path follows the eastern side of the trough as already noted in Figs. 7,8.

5. Discussion

A limitation of the study is that the geometry of the model domain is idealized and fixed to match the conditions observed in the Bellingshausen Sea and the west Antarctic Peninsula. Little et al. (2008) examined the effect of varying the shape of the continental shelf, and concluded that typical slopes $\partial H/\partial y \sim 10^{-3}$ have a relatively small impact on the melt and circulation under an ice shelf. We also note that the slope $\partial H/\partial x$ associated with the trough is relatively steep (close to 10^{-2}) and the mechanisms identified in the study should be qualitatively robust to variations in the geometry of the continental shelf. Another geometric parameter is the ice shelf itself, whose shape controls the melt rate in warm cavities by influencing the entrainment of heat in the ice-ocean boundary layer (Little et al. 2009). The general patterns of melt and circulation seem, however, to remain qualitatively the same irrespective of the ice shelf slope.

The results of this study were obtained with an eastward sbj (corresponding to conditions in western Antarctica) and may differ from those with a westward sbj (free waves propagate toward the west in Antarctica and this contributes to asymmetries in the dynamics). Moreover, the third mechanism identified (wave-topography interaction) is resolution dependent and unlikely to be captured in the global models used to estimate sea level rise. Further work would be required to fully understand the third mechanism and to ultimately parameterize its contribution to onshore heat transport in coarse global models.

Another simplification made in the study is the neglection of surface fluxes over the open ocean. In presence of significant vertical mixing, surface fluxes can cool down the deep warm inflows coming from the shelf break. Surface fluxes can also contribute to increase the basal melt of ice shelves in certain cases. Hattermann et al. (2012) report waters warmed by solar radiation intruding underneath the Fimbul ice shelf in the eastern Weddell Sea.

6. Summary and Conclusions

The objective of this study is to describe mechanisms responsible for heat exchanges within a trough on the Antarctic continental shelf. Three different mechanisms are identified: (1) a meridional melt-driven flow within the trough, (2) the interaction of the mean flow with the topography, and (3) the interaction of a Rossby wave with the topography (corresponding to mechanisms 6, 2, 4 of Klinck and Dinniman (2010) respectively; see Introduction). These mechanisms are not exclusive and may occur simultaneously (e.g. Run #7) and compete with each other.

It is worthwhile noting that these mechanisms explain a number of features seen in observations. For mechanisms 2 and 3, the main pathway for onshore heat transport is the eastern side of the trough (e.g., Moffat et al. 2009). Also, the ROMS simulations show warm anticyclones produced at the entrance of the trough every 6.5 days, as in the observations (four times per month).

The forcing is held constant in all the simulations and the time-variability described (notably the 6.5 days timescale) corresponds to the internal variability of the system. This represents a new interpretation for the timescale of the intrusions observed by Moffat et al. (2009). An alternate explanation was suggested by Dinniman et al. (2011) who showed from realistic simulations at 4 km resolution a significant correlation between the intrusions and the local winds. Additional numerical simulations that combine winds and eddy-resolving resolutions will be necessary to reconcile these results.

The onshore heat transport was also estimated for each of the simulations. An important result is that any of the three mechanisms leads to a significant circulation of slope water and a substantial onshore heat transport ($O(10^{12})$ GW). This is comparable to observations (Walker et al. 2007) and equivalent to 1 GW per km of coastline assuming one large trough per 1000 km.

Acknowledgments.

This research was supported by the National Science Foundation under Grant OCE–0927797. Three anonymous reviewers provided helpful comments that substantially improved the manuscript.

REFERENCES

Allen, S. E. and B. M. Hickey, 2010: Dynamics of advection-driven upwelling over a shelf break submarine canyon. *J. Geophys. Res.*, **115 (C08018)**, doi:10.1029/2009jc005731.

Cavalieri, D., T. Markus, and J. Comiso, 2004: AMSR-E/Aqua daily L3 12.5 km brightness temperature, sea ice concentration, & snow depth. Polar grids V002 for 2010. Boulder, Colorado USA: National Snow and Ice Data Center.

Dinniman, M. S. and J. M. Klinck, 2004: A model study of circulation and cross-shelf exchange on the west Antarctic Peninsula continental shelf. *Deep-Sea Res.*, **51**, 2003–2022, doi:10.1016/j.dsr2.2004.07.030.

Dinniman, M. S., J. M. Klinck, and W. O. Smith Jr., 2003: Cross-shelf exchange in a model of the Ross Sea circulation and biogeochemistry. *Deep-Sea Res.*, **50**, 3103–3120, doi:10.1016/j.dsr2.2003.07.011.

Dinniman, M. S., J. M. Klinck, and W. O. Smith Jr., 2007: Influence of sea ice cover and icebergs on circulation and water mass formation in a numerical circulation model of the Ross Sea, Antarctica. *J. Geophys. Res.*, **112 (C11013)**, doi:10.1029/2006JC004036.

Dinniman, M. S., J. M. Klinck, and W. O. Smith Jr., 2011: A model study of Circumpolar Deep Water on the west Antarctic Peninsula and Ross Sea continental shelves. *Deep Sea Res. II*, **58**, 1508–1523, doi:10.1016/j.dsr2.2010.11.013.

Fennel, W. and M. Schmidt, 1991: Responses to topographical forcing. *J. Fluid. Mech.*, **223**, 209–240.

Hattermann, T., O. A. Nøst, J. M. Lilly, and L. H. Smedsrud, 2012: Two years of oceanic observations below the Fimbul Ice Shelf, Antarctica. *Geophys. Res. Lett.*, **39 (L12605)**, doi:10.1029/2012GL051012.

Hedström, K. S., 2009: Technical manual for a coupled sea-ice/ocean circulation model (Version 3). Tech. rep., Arctic Region Supercomputing Center, Univ. Alaska Fairbanks, https://www.myroms.org/wiki/images/3/3b/Manual_2010.pdf.

Hellmer, H. H., F. Kauker, R. Timmermann, J. Determann, and J. Rae, 2012: Twenty-first-century warming of a large Antarctic ice-shelf cavity by a redirected coastal current. *Nature*, **485**, 225–228, doi:10.1038/nature11064.

Holland, D. M. and A. Jenkins, 1999: Modeling thermodynamic ice–ocean interactions at the base of an ice shelf. *J. Phys. Oceanogr.*, **29**, 1787–1800.

Holland, D. M., R. H. Thomas, B. de Young, M. H. Ribergaard, and B. Lyberth, 2008a: Acceleration of Jakobshavn Isbræ triggered by warm subsurface ocean waters. *Nat. Geosci.*, **1**, doi:10.1038/ngeo316.

Holland, P. R., A. Jenkins, and D. M. Holland, 2008b: The response of ice shelf basal melting to variations in ocean temperature. *J. Clim.*, **21**, 2558–2572, doi:10.1175/2007JCLI1909.1.

Holloway, G., 1992: Representing topographic stress for large-scale ocean models. *J. Phys. Oceanogr.*, **22**, 1033–1046.

Huppert, H. E. and K. Bryan, 1976: Topographically generated eddies. *Deep-Sea Res.*, **23**, 655–679.

Jacobs, S. S., A. Jenkins, C. F. Giulivi, and P. Dutrieux, 2011: Stronger ocean circulation and increased melting under Pine Island Glacier ice shelf. *Nat. Geosc.*, **4**, 519–523, doi:10.1038/ngeo1188.

Jenkins, A., P. Dutrieux, S. S. Jacobs, S. D. McPhail, J. R. Perrett, A. T. Webb, and

D. White, 2010: Observations beneath Pine Island Glacier in West Antarctica and implications for its retreat. *Nat. Geosci.*, **3**, doi:10.1038/NGEO890.

Jenkins, A. and S. Jacobs, 2008: Circulation and melting beneath George VI Ice Shelf, Antarctica. *J. Geophys. Res.*, **113 (C04013)**, doi:10.1029/2007JC004449.

Joughin, I., I. M. Howat, M. Fahnestock, B. Smith, W. Krabill, R. B. Alley, H. Stern, and M. Truffer, 2008: Continued evolution of Jakobshavn Isbrae following its rapid speedup. *J. Geophys. Res.*, **113 (F04006)**, doi:10.1029/2008JF001023.

Klinck, J. M. and M. S. Dinniman, 2010: Exchange across the shelf break at high southern latitudes. *Ocean Sci.*, **6**, 513–524, doi:10.5194/os-6-513-2010.

Klinck, J. M., E. E. Hofmann, R. C. Beardsley, B. Salihoglu, and S. Howard, 2004: Water-mass properties and circulation on the west Antarctic Peninsula Continental Shelf in Austral Fall and Winter 2001. *Deep-Sea Res.*, **51**, 1925–1946, doi:10.1016/j.dsr2.2004.08.001.

Little, C. M., A. Gnanadesikan, and R. Hallberg, 2008: Large-scale oceanographic constraints on the distribution of melting and freezing under ice shelves. *J. Phys. Oceanogr.*, **38**, 2242–2255, doi:10.1175/2008JPO3928.1.

Little, C. M., A. Gnanadesikan, and M. Oppenheimer, 2009: How ice shelf morphology controls basal melting. *J. Geophys. Res.*, **114 (C12007)**, doi:10.1029/2008JC005197.

Martinson, D. G. and D. C. McKee, 2012: Transport of warm Upper Circumpolar Deep Water onto the western Antarctic Peninsula continental shelf. *Ocean Science*, **8**, 433–442, doi:10.5194/os-8-433-2012.

Moffat, C., B. Owens, and R. C. Beardsley, 2009: On the characteristics of Circumpolar Deep Water intrusions on the west Antarctic Peninsula Continental Shelf. *J. Geophys. Res.*, **114 (C05017)**, doi:10.1029/2008JC004955.

NCAR, 2010: The Antarctic Mesoscale Prediction System (AMPS). NCAR, http://www.mmm.ucar.edu/rt/amps/.

Nicholls, K. W., S. Østerhus, K. Makinson, T. Gammelsrød, and E. Fahrbach, 2009: Ice-ocean processes over the continental shelf of the Southern Weddell Sea, Antarctica: A review. *Rev. of Geophys.*, **47 (rg3003)**, 23, doi:10.1029/2007rg000250.

Nick, F. M., A. Vieli, I. M. Howat, and I. Joughin, 2009: Large-scale changes in Greenland outlet glacier dynamics triggered at the terminus. *Nat. Geosci.*, **2**, doi:10.1038/NGEO394.

Nøst, O. A., M. Biuw, V. Tverberg, C. Lydersen, T. Hattermann, Q. Zhou, L. H. Smedsrud, and K. M. Kovacs, 2011: Eddy overturning of the Antarctic Slope Front controls glacial melting in the eastern Weddell Sea. *J. Geophys. Res.*, in press.

Nycander, J. and K. Döös, 2003: Open boundary conditions for barotropic waves. *J. Geophys. Res.*, **108 (C5-3168)**, doi:10.1029/2002JC001529.

Payne, A. J., A. Vieli, A. P. Shepherd, D. J. Wingham, and E. Rignot, 2004: Recent dramatic thinning of largest west antarctic ice stream triggered by oceans. *Geophys. Res. Lett.*, **31 (L23401)**, doi:10.1029/2004GL021284.

Prézelin, B. B., E. E. Hofmann, C. Mengelt, and J. M. Klinck, 2000: The linkage between Upper Circumpolar Deep Water (UCDW) and phytoplankton assemblages on the west Antarctic Peninsula continental shelf. *J. Mar. Res.*, **58**, 165–202.

Pritchard, H. D., R. J. Arthern, D. G. Vaughan, and L. A. Edwards, 2009: Extensive dynamic thinning on the margins of the Greenland and Antarctic ice sheets. *Nature*, **461**, 971–975, doi:10.1038/nature08471.

Rignot, E., I. Velicogna, M. R. van den Broeke, A. Monaghan, and J. Lenaerts, 2011: Acceleration of the contribution of the Greenland and Antarctic ice sheets to sea level rise. *Geophys. Res. Lett.*, **38 (L05503)**, doi:10.1029/2011GL046583.

Shchepetkin, A. F. and J. C. McWilliams, 2008: Computational kernel algorithms for fine-scale, multi-process, long-time oceanic simulations. *Handbook of Numerical Analysis, Vol. XIV: Computational Methods for the Ocean and the Atmosphere*, P. G. Ciarlet, R. Temam, and J. Tribbia, Eds., Elsevier Science, Vol. 14, 121–183, doi:10.1016/S1570-8659(08)01202-0.

Steig, E. J., Q. Ding, D. S. Battisti, and A. Jenkins, 2012: Tropical forcing of Circumpolar Deep Water inflow and outlet glacier thinning in the Amundsen Sea embayment, West Antarctica. *Annals of Glaciology*, **53 (60)**, doi:10.3189/2012AoG60A110.

Sverdrup, H. U., 1953: The currents off the coast of Queen Maud Land. *Særtrykk av Norsk Geografisk Tidsskrift*, **14**, 239–249.

Wåhlin, A. K., X. Yuan, G. Björk, and C. Nohr, 2010: Inflow of warm Circumpolar Deep Water in the central Amundsen Shelf. *J. Phys. Oceanogr.*, **40**, 1427–1434, doi:10.1175/2010JPO4431.1.

Walker, D. P., M. A. Brandon, A. Jenkins, J. T. Allen, J. A. Dowdeswell, and J. Evans, 2007: Oceanic heat transport onto the Amundsen Sea shelf through a submarine glacial trough. *Geophys. Res. Lett.*, **34 (L02602)**, doi:10.1029/2006GL028154.

Zhang, Y., J. Pedlosky, and G. R. Flierl, 2011a: Cross-shelf and out-of-bay transport driven by an open-ocean current. *J. Phys. Oceanogr.*, **41**, 2168–2186, doi:10.1175/JPO-D-11-08.1.

Zhang, Y., J. Pedlosky, and G. R. Flierl, 2011b: Shelf circulation and cross-shelf transport out of a bay driven by eddies from an open-ocean current. Part I: Interaction between a barotropic vortex and a steplike topography. *J. Phys. Oceanogr.*, **41**, 889–910, doi:10.1175/2010jpo4496.1.

List of Tables

TABLE 1. Numerical simulations conducted in the study. $\overline{u}\,H$ is the depth-integrated velocity of the longshore flow, y(jet) is the position of the shelf break jet, and Δx the grid resolution.

Run #	Trough	Thermo.	$\overline{u}H$ ($\mathrm{m^2\ s^{-1}}$)	y(jet) (km)	Δx (km)	Duration (Days)	Short Name
1	No	Yes	300	218	1	59	No trough
2	Yes	Yes	—	—	1	143	No jet
3	Yes	No	90	206	1	40	Wide jet
4	Yes	No	90	206	3	200	Wide jet 3 km
5	Yes	No	300	218	1	210	No thermo
6	Yes	No	300	218	3	347	No thermo 3 km
7	Yes	Yes	300	218	1	347	Control run
11	Yes	No	300	218	2	347	No thermo 2 km
13	Yes	No	300	223	1	91	5 km seaward
14	Yes	No	300	228	1	91	10 km seaward
15	Yes	No	200	218	1	85	Slow jet 1
16	Yes	No	100	218	1	85	Slow jet 2

List of Figures

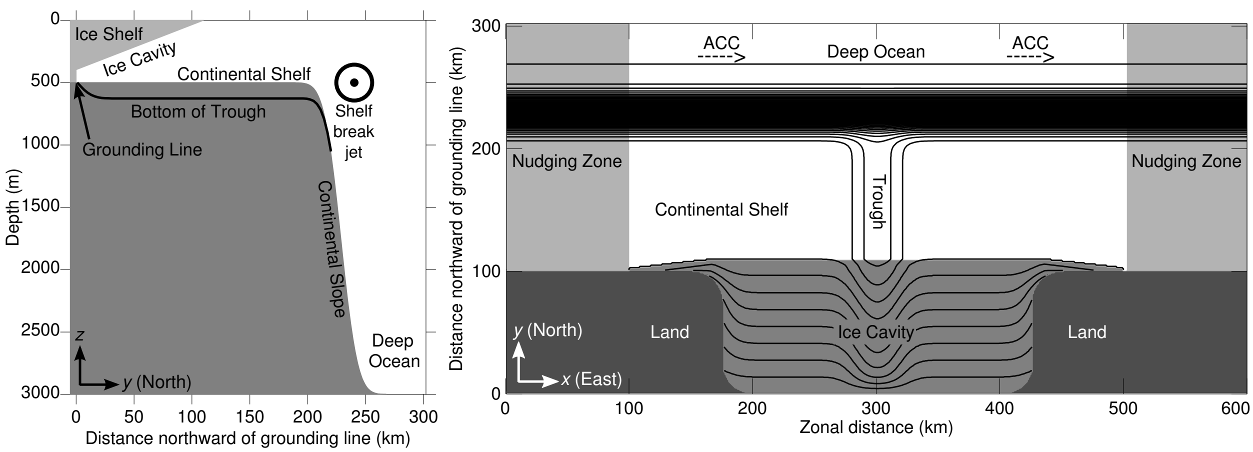

FIG. 1. Geometry of the idealized ice shelf-coastal domain. (Left) Side view. (Right) Top view. The contour lines are the thickness of the water column (interval 50 m).

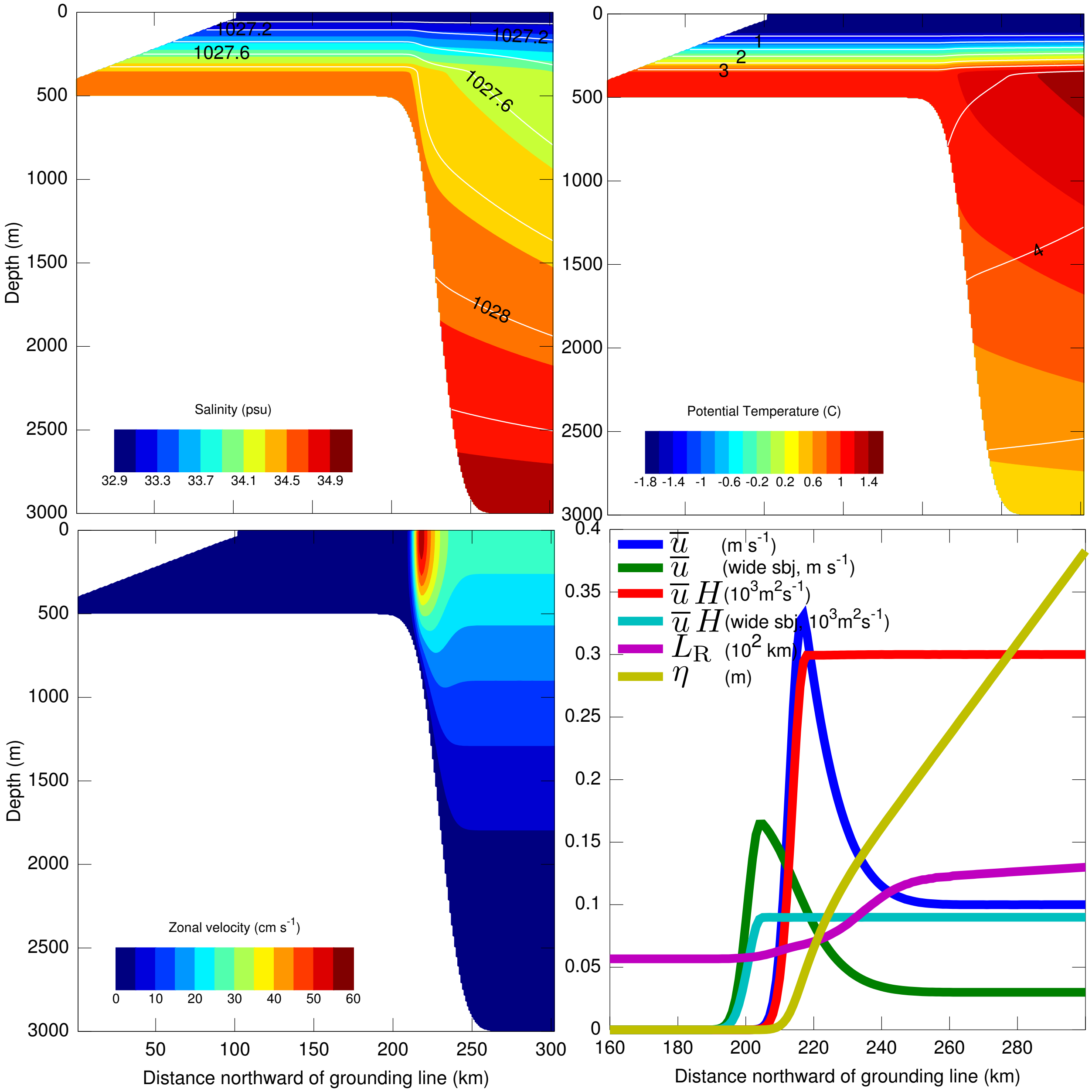

FIG. 2. Initial and boundary conditions used in Runs #1,5,6,7,11. (Top left) Salinity S and neutral density γ (contour lines). (Top right) Potential temperature θ and temperature T above *in situ* freezing point (contour lines). (Bottom left) Zonal velocity (positive eastward/out of the page). (Bottom right) Cross-shelf variation of various parameters. See text for definition of symbols.

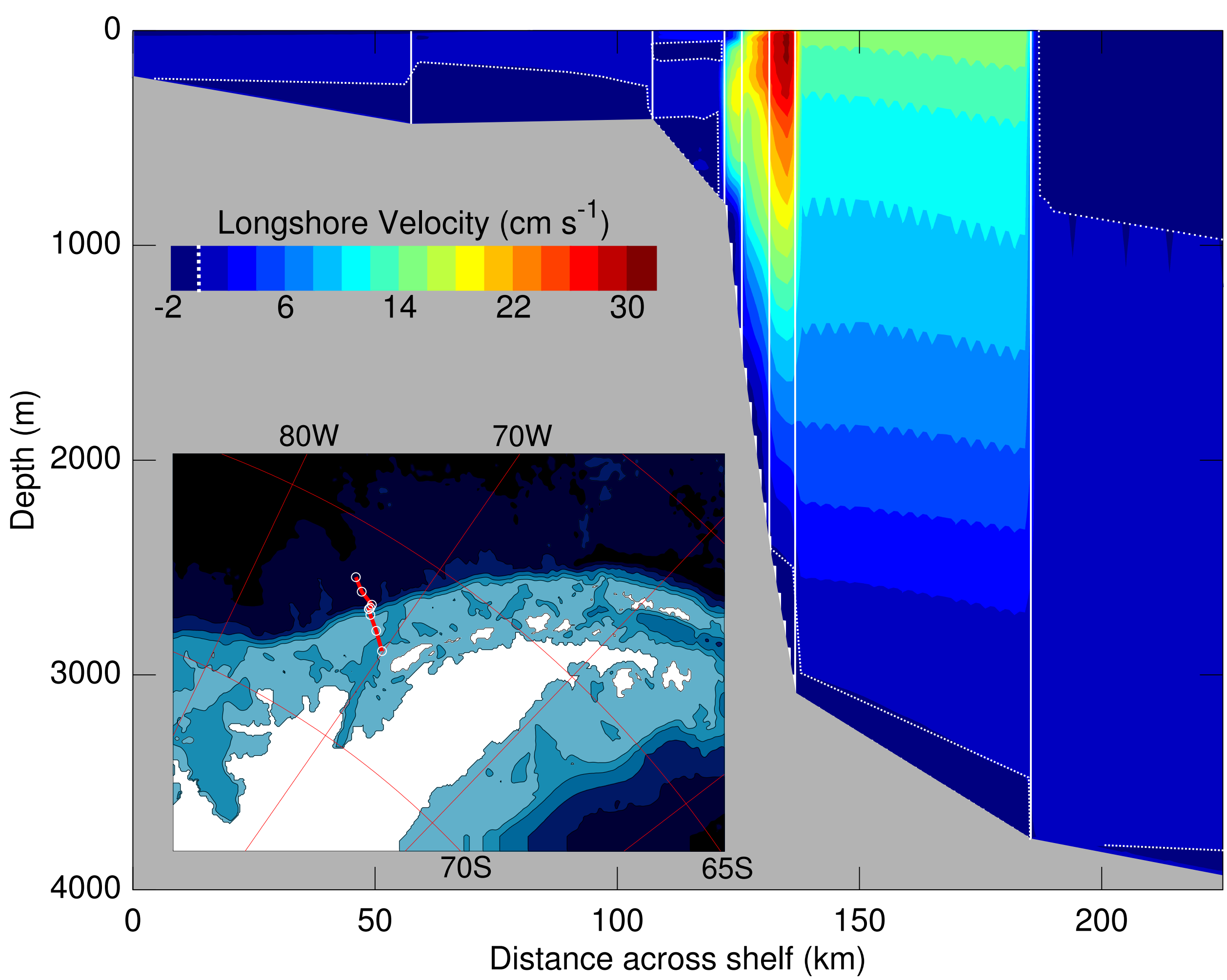

FIG. 3. Geostrophic jet along the shelf break of the Bellingshausen Sea. Profiles are from the World Ocean Circulation Experiment (WOCE, February 1992, transect S04P) and shown as solid vertical white lines. Velocities are assumed zero at the bottom. Positive values are out of the page (northeastward). The location of the profiles is shown in the inset.

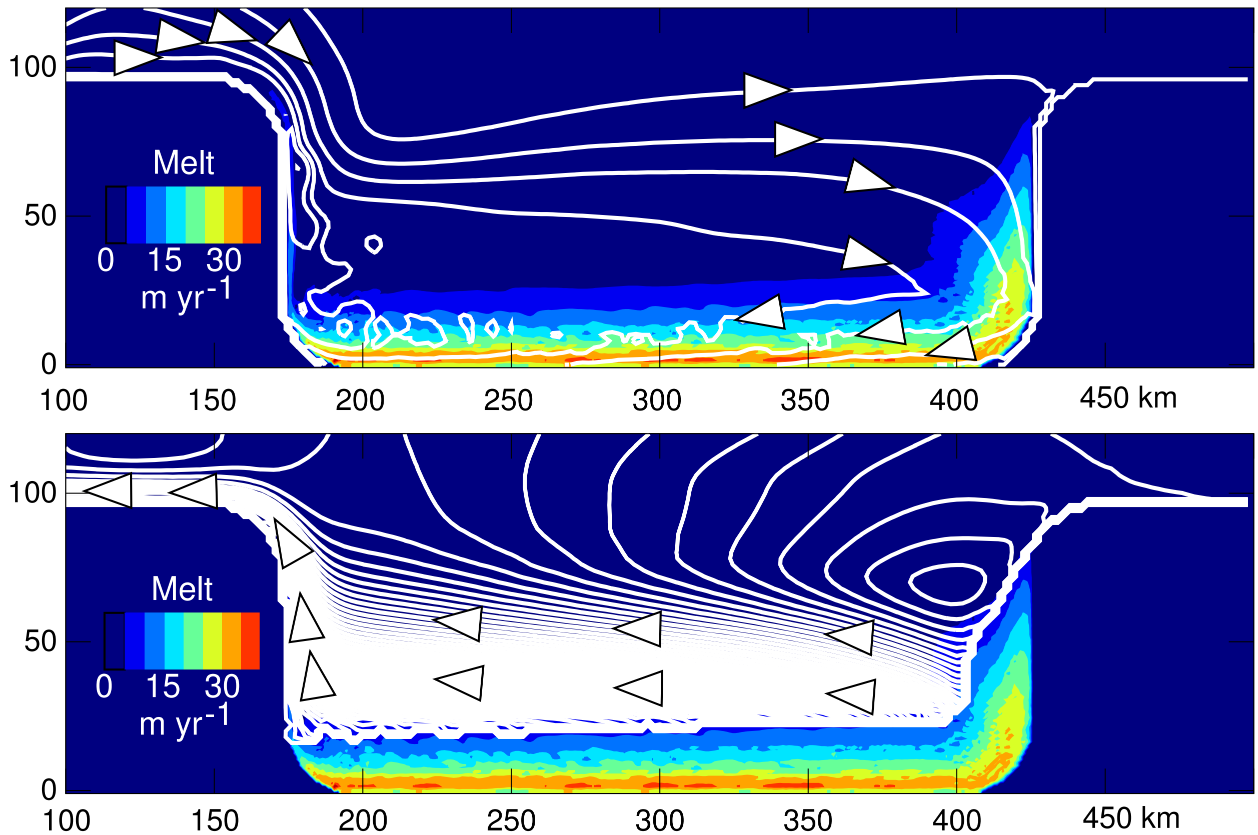

Fig. 4. (Top) Mean circulation over a deep isopycnal ($\gamma_2 \equiv 1027.8\,\mathrm{kg\,m^{-3}}$, $z \sim -300\,\mathrm{m}$) for the case with no trough (Run #1). The contour interval for the streamlines is $10^2\,\mathrm{m^2\,s^{-1}}$. The mean basal melt rate is shaded in color. (Bottom) Same as above but over a density surface grazing the base of the ice shelf ($\gamma_1 \equiv 1027.3\,\mathrm{kg\,m^{-3}}$). Note that this isopycnal intersects with the ice shelf at $y \approx 20\,\mathrm{km}$.

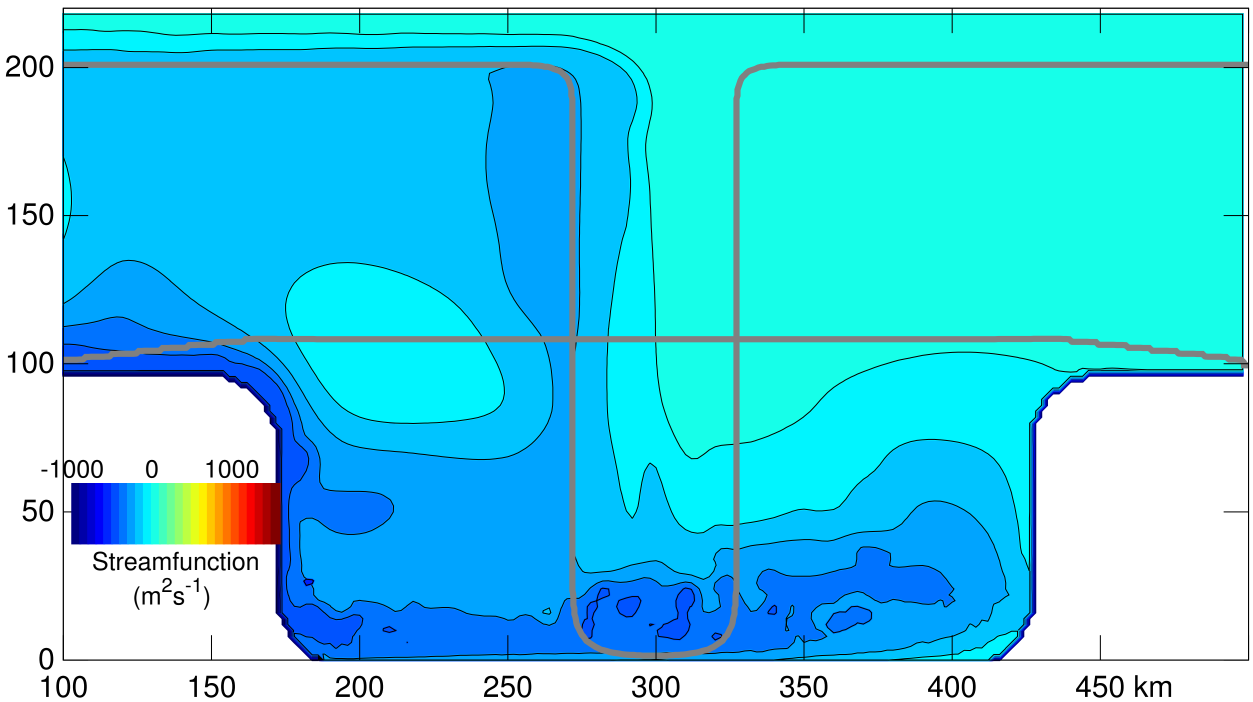

FIG. 5. Mean circulation over the deep isopycnal γ_2 in the case with a trough and no shelf break jet (Run #2). The contour interval for the streamfunction ψ is $10^2\ \mathrm{m^2\,s^{-1}}$ and the flow is to the right of $\boldsymbol{\nabla}\psi$. The gray lines give the extent of the trough and that of the ice shelf.

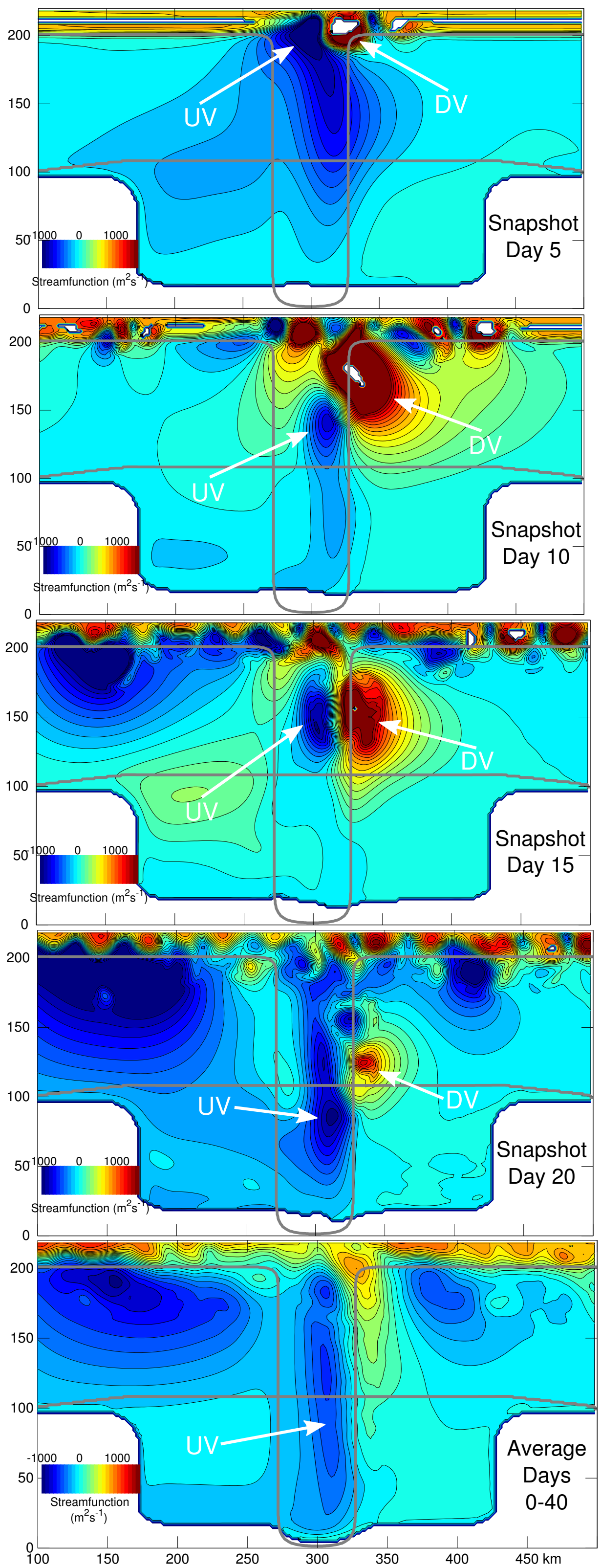

FIG. 6. As in Fig. 5 but for the case with a wide shelf break jet and no thermodynamics (Run #3). White areas are where the isopycnal outcrops the bottom. UV (DV) means Upstream (Downstream) Vortex.

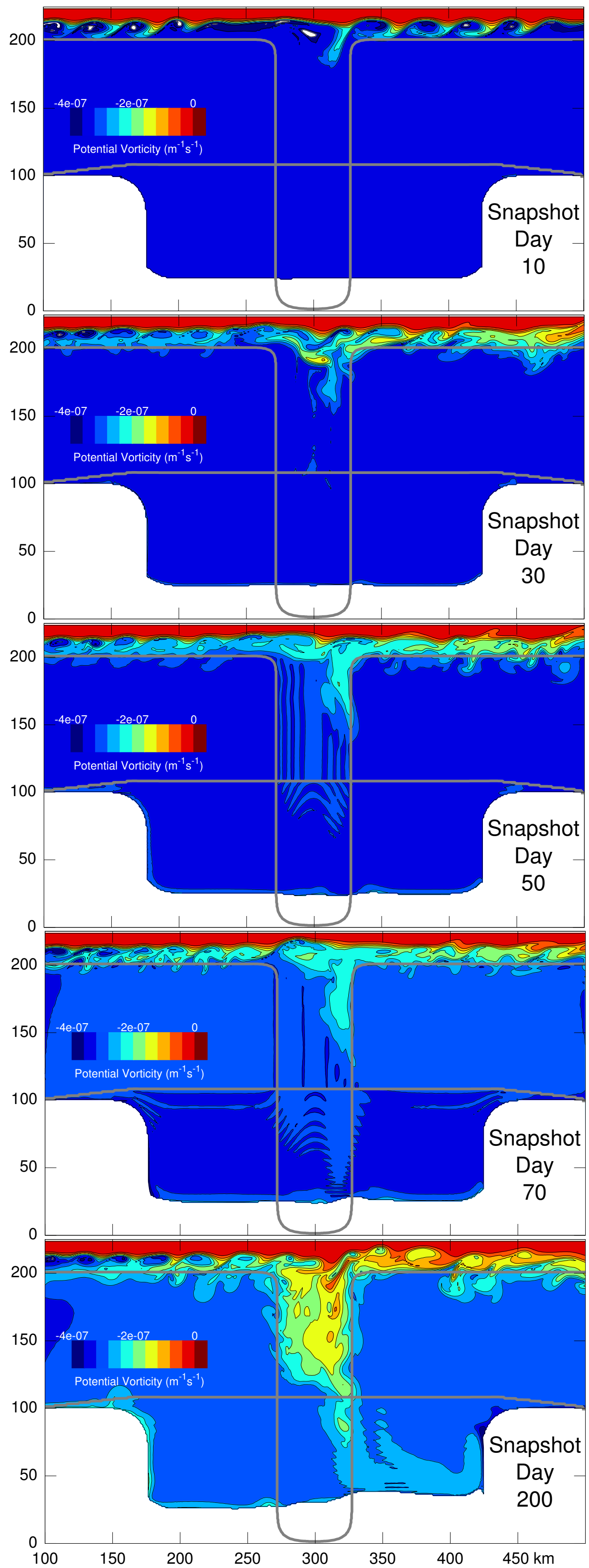

FIG. 7. Potential vorticity q of the deep isopycnal γ_2 for the case with a shelf break jet and no thermodynamics (Run #5). The gray lines give the extent of the trough.

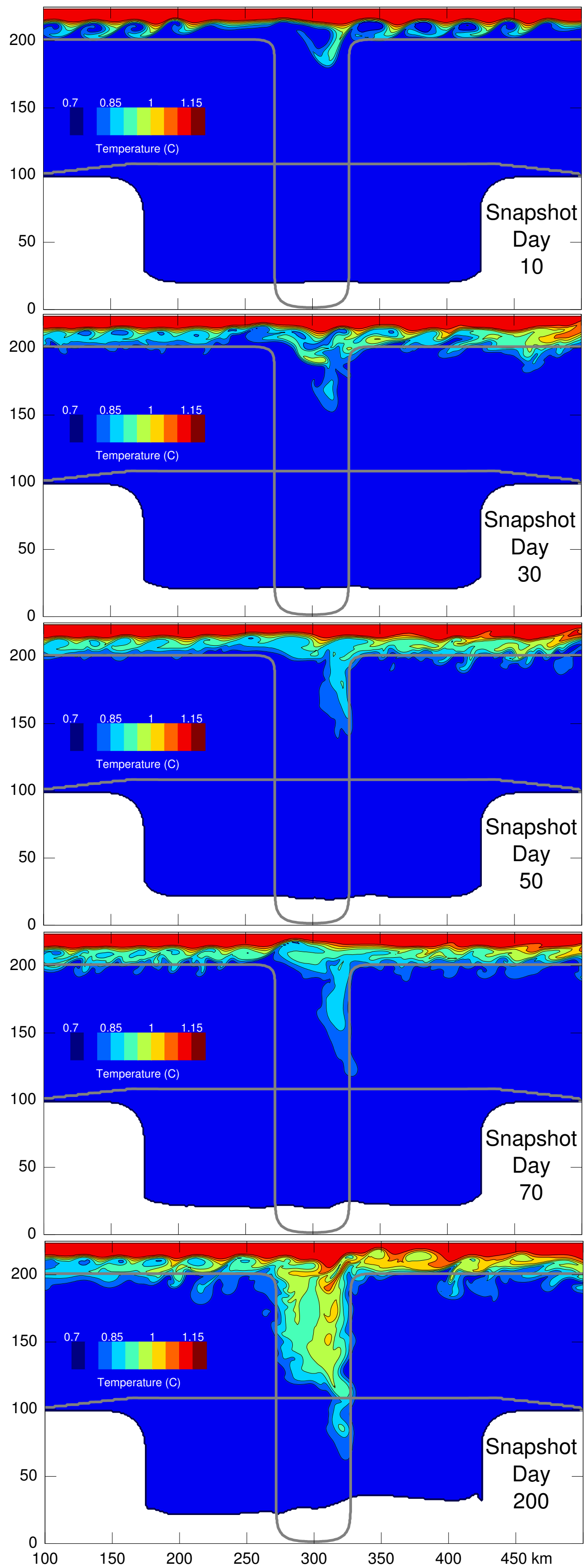

FIG. 8. Potential temperature θ of the deep isopycnal γ_2 for the case with a shelf break jet and no thermodynamics (Run #5). The gray lines give the extent of the trough.

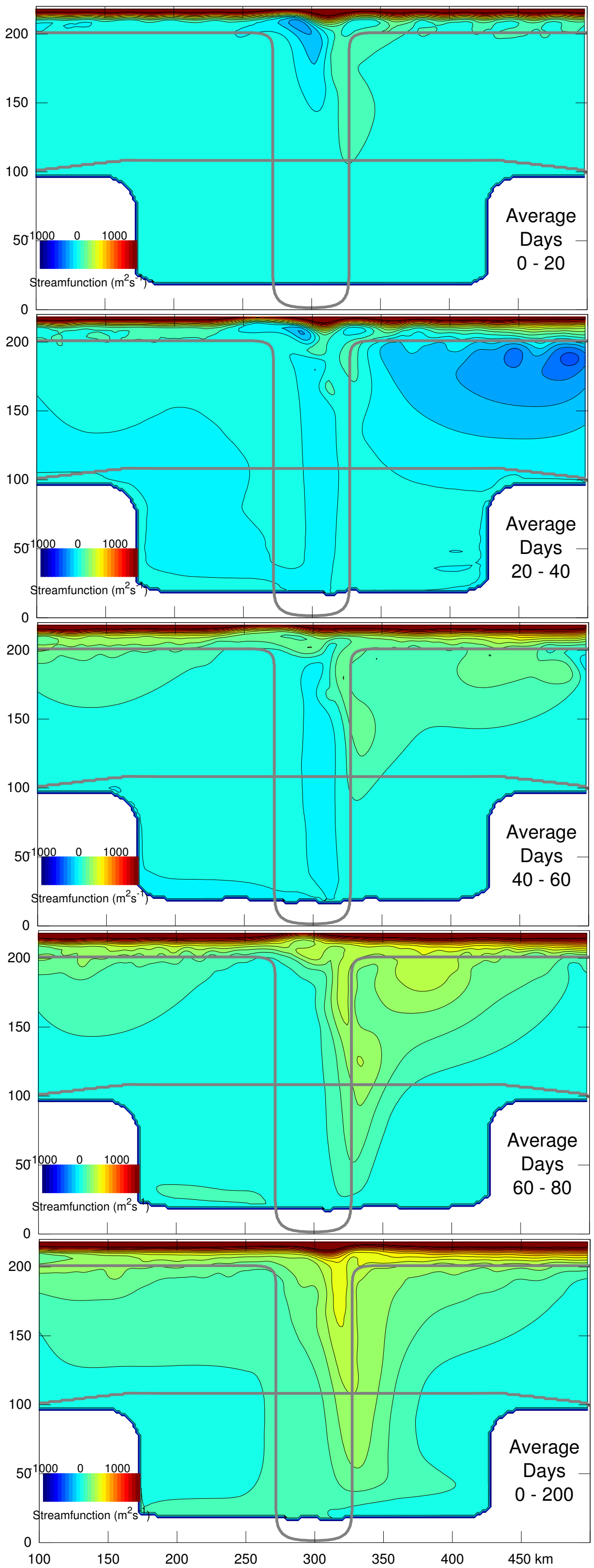

FIG. 9. As in Fig. 5 but for the case with a shelf break jet and no thermodynamics (Run #5).

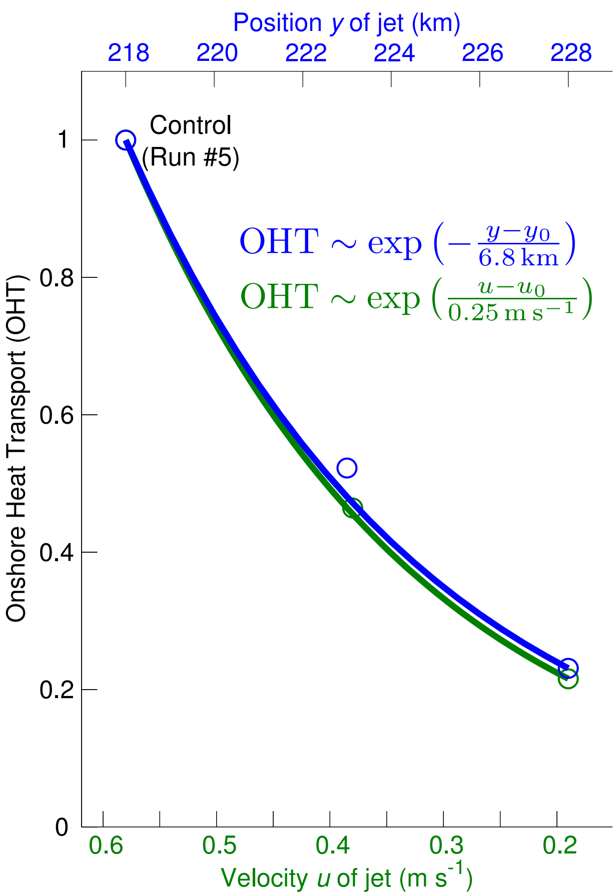

FIG. 10. Sensitivity of mean Onshore Heat Transport (OHT) to the position and velocity of the jet (Mechanism 3; Runs #5,13–16). The transport is non-dimensionalized by its value from the control simulation (Run #5). The solid lines are exponential regressions to the data points. The Rossby radius of deformation is 6.9 km at $y = 220$ km.

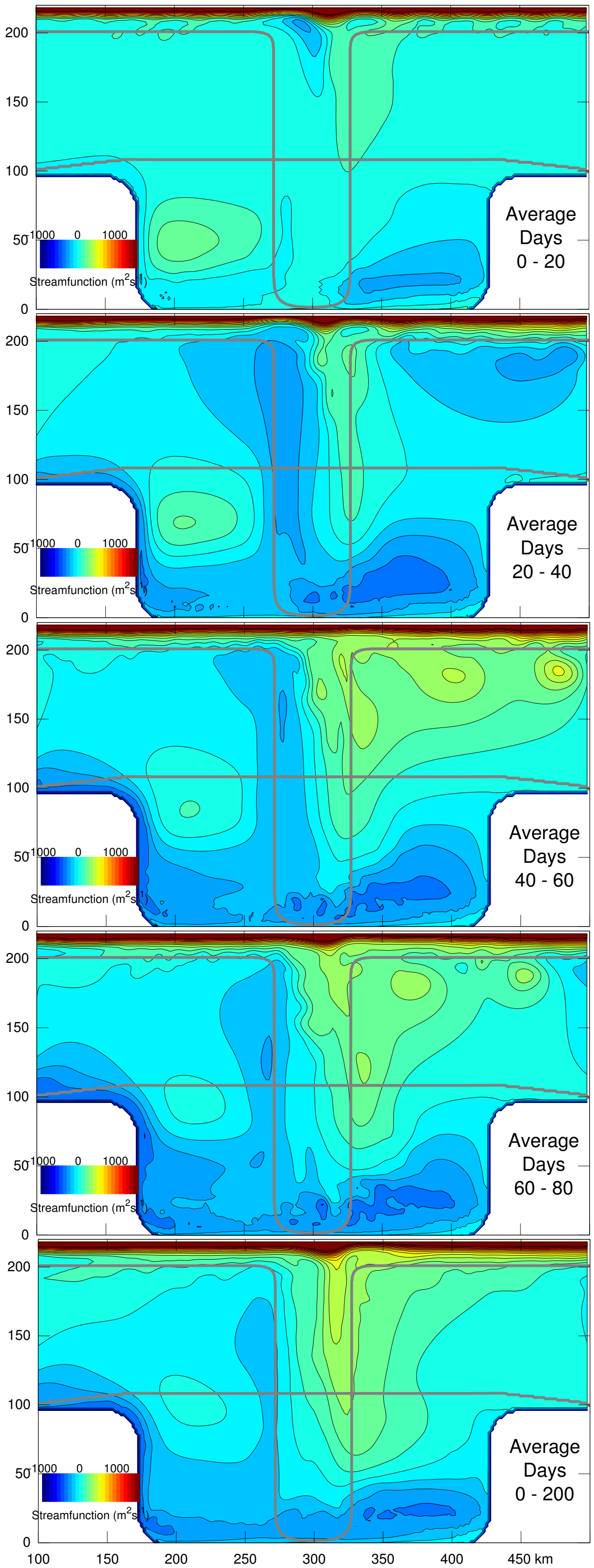

FIG. 11. As in Fig. 5 but for the case with a shelf break jet and thermodynamics (Run #7).

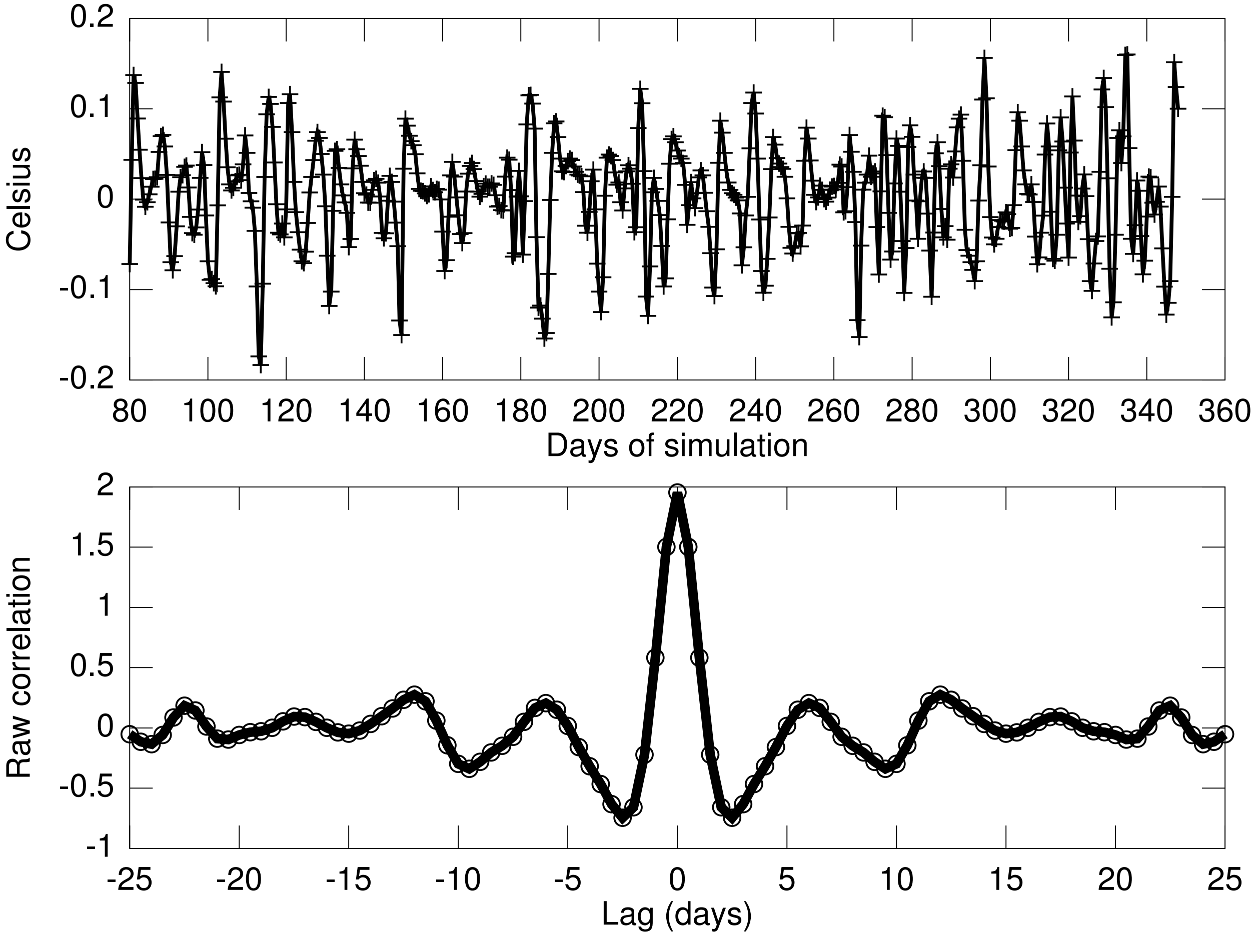

FIG. 12. (Top) Temperature anomaly at 300 m at the entrance of the trough. The sampling interval is 0.5 days. (Bottom) Lagged-correlation of the temperature anomaly timeseries with itself. Correlation is high for lags $\mathsf{T}_i = \pm 6.5\, n$ days with $n = 0, 1, 2, ...$

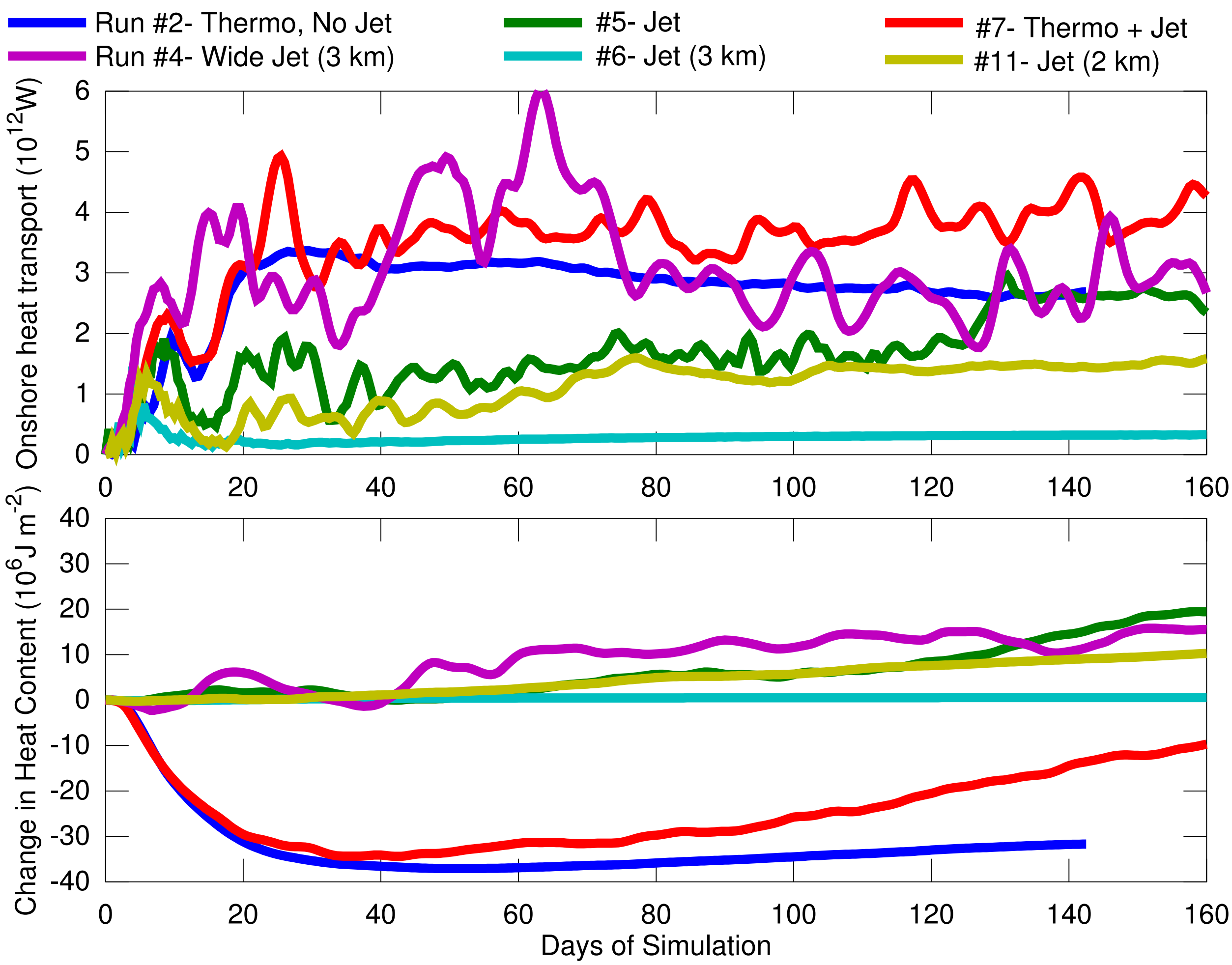

FIG. 13. (Top) Onshore heat transport at the entrance of the cavity (y = 99 km; the transport is relative to *in situ* freezing point). (Bottom) Change in heat content over the continental shelf including the ice cavity ($0 < y < 180$ km). The numbers in the legend refer to the run numbers (see Table 1).

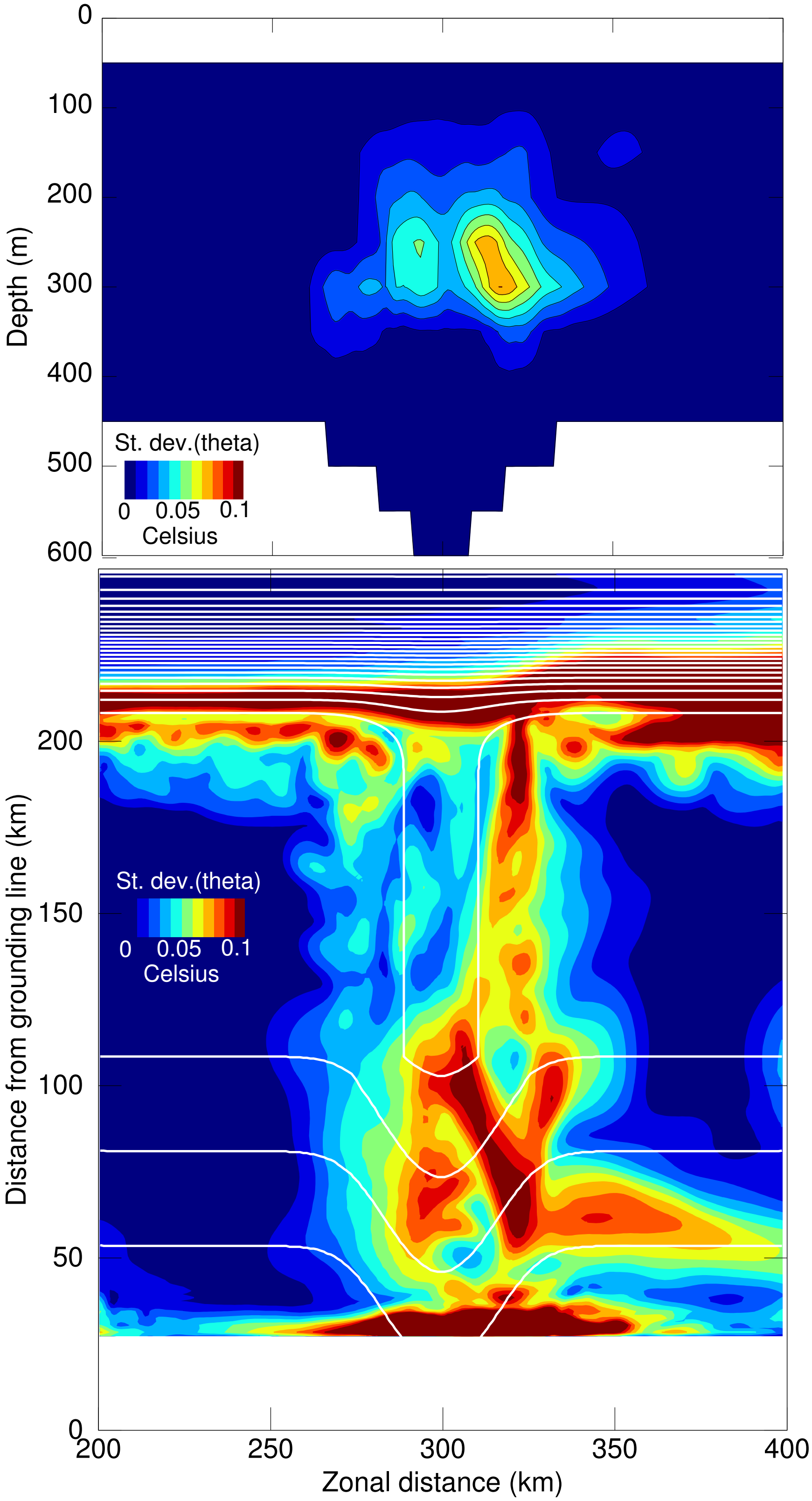

FIG. 14. (Top) Standard deviation of potential temperature θ across the plane $y = 155\,\mathrm{km}$. The 'steps' in the bathymetry are plotting artefacts and the model bathymetry is actually smooth. (Bottom) Same as above but at 300 m. White contour lines are water column thickness (interval 100 m). Results are averaged over days 153–279 (Run #7).